Electronic Supplementary Material (ESI) for Journal of Materials Chemistry A.

Supporting Information

Carbon quantum dots sensitized integrated Fe_2O_3@g-C_3N_4 core-shell nanoarrays photoanode towards highly efficient water oxidation

1. Experimental section

1.1 Chemicals and materials: Urea (CH_4N_2O), potassium acid phosphate (KH_2PO_4, >99.5%), dipotassium hydrogen phosphate trihydrate ($K_2HPO_4{\cdot}3H_2O$, >99%), dicyandiamide ($C_2H_4N_4$) and hydrogen peroxide aqueous solution (H_2O_2, 30%) were bought from Sinopharm Chemical Reagent Co., Ltd. Titanium tetrachloride ($TiCl_4$, >99.5%) and potassium hydroxide (KOH, >90%) were obtained from Aladdin Reagent Co., Ltd. Ferric chloride ($FeCl_3$, >99%) was supplied by Tianjin East China Reagent Factory. Sucrose ($C_{12}H_{22}O_{11}$) was obtained from Beijing Chemical Works. Anhydrous sodium sulfite (Na_2SO_3, >97%) were purchased from Tianjin Guangfu Fine Chemical Research Institute Co., Ltd. Fluorine-doped tin oxide glass ($F:SnO_2$, FTO, <15 ohm sq^{-1}) was purchased from Zhuhai Kaivo Optoelectronic Technology Co., Ltd, and ultrasonically cleaned by sonication in acetone, ethanol and water, respectively, for 15 min and dried with Ar flow before experiment. Deionized water (18.2 MΩ·cm) provided by reverse osmosis followed by ion-exchange and filtration was used in the whole experimental processes. All chemicals used in this study were of analytical grade and used without any purification.

1.2 Preparation of Fe_2O_3 and Ti-doped Fe_2O_3 films: a titanium-doped hematite (**$Ti:Fe_2O_3$**) film was prepared by a calcination-assisted hydrothermal method. Thus, a 25 mL of prepared homogeneous saffron yellow colored solution containing 0.1 M $FeCl_3$ and 0.15 M urea was achieved by stirring for 15 min. Then, a certain volume of Ti precursor solution (1% $TiCl_4$ ethanol, volume percentage) was added as dopant with a Fe:Ti atomic ratio of 0.995:0.005 for 0.5% Ti concentration. The obtained solution was transferred to a 40-mL Teflon-lined stainless autoclave and also a piece of FTO (1 cm × 2.5 cm) was slide into the autoclave with its

conducting side facing down. The autoclave was maintained at 100°C for 4 h to form uniform layer of Ti-doped iron oxyhydroxide (Ti:FeOOH) on the FTO substrate. After fully wash and drying, the film was annealed at 550℃ for 2 h and at 660℃ for an additional 20 min in air atmosphere with a heating rate of 2°C min^{-1}. The final product was labeled as 0.5 at% Ti:Fe_2O_3. To obtain various atomic ratio of Ti doped Fe_2O_3 (0, 0.1, 0.3, and 0.7 at%), similarly, a series of certain volumes of Ti precursor were dropped into the final solution.

1.3 Preparation of carbon quantum dots (CQDs): CQDs were synthesized using a pyrolysis method. A 20 mL (0.07 M) of sucrose aqueous solution was prepared as a precursor solution. Afterwards, the above solution was transferred to a 40-mL Teflon-lined stainless autoclave and heated at 180℃ for 5 h. Finally, the CQDs solution was achieved by drawing the upper clear solution, and the concentration was measured to be 12.5 mg mL^{-1}.

1.4 Preparation of g-C_3N_4 nanosheets modified Ti:Fe_2O_3 (Ti:Fe_2O_3@GCNNs), CQDs modified Ti:Fe_2O_3 (Ti:Fe_2O_3/CQDs), and Ti:Fe_2O_3@GCNNs-CQDs: the GCNNs was deposited on Ti:Fe_2O_3 by utilizing a chemical vapor phase deposition method in air atmosphere with dicyandiamide as a precursor. Varying weights of dicyandiamide (0.125, 0.25, and 0.5 g) were placed on the bottom of the crucible with a cover, and the Ti:Fe_2O_3 films were suspend in above the dicyandiamide about 1 cm. Then Ti:Fe_2O_3@GCNNs with various loading amounts of GCNNs could be achieved by sintering at 550℃ for 3 h with a heating rate of 2°C min^{-1}. Similar procedure was used to prepare the GCNNs/FTO sample. Meanwhile, bulk g-C_3N_4 was achieved on the bottom of the crucible. For achieving GCNNs solution, the GCNNs/FTO sample was sonicated in deionized water for 30 min. For the synthesis of Ti:Fe_2O_3/CQDs and Ti:Fe_2O_3@GCNNs-CQDs, the simple spin-coating strategy was utilized. Briefly, a series of volumes of CDQs solution (10, 20, and 30 μL) were dipped on the Ti:Fe_2O_3 (or

Ti:Fe_2O_3@GCNNs) films surface with a transfer liquid gun, and spin coated at 3000 rpm for 20 s, followed by drying at 100°C.

1.5 Characterization: room temperature photoluminescence (PL) spectra were obtained on a RF-5301 (Shimadzu). The X-ray diffraction (XRD) patterns were recorded on a Rigaku RINT-2000 diffractometer with Cu Kα radiation (λ = 1.54056 Å). The X-ray photoelectron spectroscopy (XPS) spectra were performed on a Thermo VG Scientific ESCALAB 250 spectrometer using monochromatized Al Kα excitation. All binding energies were corrected for sample charging effect with reference to the C 1s line at 284.6 eV. Raman spectra were measured on a micro-Raman spectrometer (Renishaw, laser wavelength 532 nm). Ultraviolet-visible diffuse reflectance spectra (UV-vis DRS) were recorded on a UV-vis-NIR spectrophotometer (Shimadzu UV-3600) over the range of 300-800 nm. Transmission electron microscope (TEM, Tecnai F20, Philips) and corresponding scanning TEM-energy-dispersive X-ray spectrometry (STEM-EDX) elemental mapping were applied for the detailed microstructure and composition analyses. Field-emission scanning electron microscopy (FESEM) was applied on a field emission scanning electron microscope (JEOL6700F).

1.6 Photoelectrochemical (PEC) measurements: PEC performance of the as-prepared photoelectrodes were all collected by an electrochemical analyzer (CHI760E) in a three-electrode configuration, with the prepared photoanode films, Pt wire and Ag/AgCl (saturated KCl solution) as the working, counter and reference electrodes, respectively. 1 M KOH aqueous solution (pH 13.6) was used as the electrolyte. The light was provided by a 300 W Xenon arc lamp (CEL-HXF 300, $320 < \lambda < 780$ nm) equipped with an AM 1.5G filter and the light intensity at the photoanode surface was adjusted to 100 mW cm^{-2} (1 sun illumination). The illuminated area was 0.38465 cm^2. At room temperature, the applied bias was converted

to the reversible hydrogen electrode (RHE) using the following Nernst equation (S1):[10]

$$E_{RHE} = E_{Ag/AgCl} + E_{Ag/AgCl}^{0} + 0.0591\,V \times pH \qquad (S1)$$

$(E_{Ag/AgCl}^{0} = 0.1976\,V\ vs.NHE\ at\ 25℃)$

where E_{RHE} is the potential versus (*vs.*) RHE, $E_{Ag/AgCl}$ is the experimental potential measured *vs.* the Ag/AgCl electrode, and $E_{Ag/AgCl\ vs.\ NHE}^{0}$ is the standard potential of the Ag/AgCl *vs.* NHE (0.1976 V at 25°C). The linear-sweep voltammograms (LSV) curves were plotted at a scan rate of 50 mV s^{-1} by sweeping the potential in the positive direction. For stability measurement, the long-term amperometric photocurrent density-time (*I-t*) curve was conducted under continuous irradiation with a bias of 1.23 V_{RHE}. Potential versus time for the obtained four photoanodes were performed at the same current density of 1 mA cm^{-2} under AM 1.5G illumination. The cyclic voltammogram (CV) curve of CQDs was conducted using the bare FTO and CQDs solution (2 mg mL^{-1}) as the work electrode and the electrolyte, respectively. The electrochemical impedance spectroscopy (EIS) Nyquist plots were collected by applying an AC voltage amplitude of 5 mV within the frequency range from 10^5 to 10^{-1} Hz under an open circuit potential (OCP) condition and light irradiation (AM 1.5G, 100 mW cm^{-2}).

2. Applied bias photo-to-current efficiency: the applied bias photon-to-current efficiency (ABPE) of the solar-driven water splitting was used to quantify photoanode performance, which can be calculated based on the measured LSV curves, using the following equation (S2):[S1]

$$ABPE\ (\%) = \frac{(1.23 - V) \times J}{P} \times 100 \qquad (S2)$$

in which J is the photocurrent density (mA cm^{-2}) reads from the LSV curve, V is the applied bias (V *vs*. RHE), and P is the incident light density (100 mW cm^{-2}).

3. Incident photon-to-current efficiency: the incident photon-to-current efficiency (IPCE) was performed under monochromatic irradiation from a 300 W Xenon arc lamp coupled with a monochromator (Zolix, Omni-λ 300) at 1.23 V_{RHE} according to the equation (S3):[21]

$$IPCE\ (\%) = \frac{1240\, J_{ph}(\lambda)}{P\,(\lambda)\lambda} \times 100 \qquad (S3)$$

where $J_{ph}(\lambda)$, λ, and P(λ) are photocurrent density (mA cm^{-2}), wavelength of light (nm), and power density of monochromatic light (mW cm^{-2}) which was measured by a calibrated Si detector, respectively.

4. Absorbed photon-to-current efficiency: absorbed photon-to-current efficiency (APCE) was determined at each wavelength by dividing the IPCE by the light harvesting efficiency (LHE) according to the following equations (S4-S5):[10,21]

$$APCE\ (\%) = \frac{IPCE\ (\%)}{LHE} \qquad (S4)$$

$$LHE = 1 - 10^{-A(\lambda)} \qquad (S5)$$

in which A(λ) is the absorbance at wavelength λ.

5. Mott-Schottky analysis: the Mott-Schottky (M-S) plots were generated under dark with a voltage of 5 mV at a frequency of 1 kHz. In the M-S plot, the flat band potential of the photoelectrode is measured according to following equation (S6):[24,S2]

$$\frac{1}{C^2} = \frac{2}{e\varepsilon\varepsilon_0 N_D}\left[(V - V_{fb}) - \frac{\kappa T}{e}\right] \qquad (S6)$$

in which C is the space charge capacitance, e is the electron charge, ε is the vacuum permittivity (8.85×10^{-12} F m^{-1}), ε_0 is the relative dielectric constant of hematite ($\varepsilon_0 = 80$),[25] N_D is the charge donor density (cm^{-3}), V is the electrode applied potential, V_{fb} is the flat band potential, κ is the Boltzmann's constant (1.38×10^{-23} J K^{-1}) and T is the absolute temperature (in K).

In addition, the slopes determined from the analysis of M-S plots were applied to calculate the carrier density by the following equation (S7):[S2]

$$N_D = \frac{2}{e\varepsilon\varepsilon_0}\left[\frac{d\left(\frac{1}{C^2}\right)}{dV}\right]^{-1} \qquad (S7)$$

Here, we should notice that the capacitance (C) obtained from equation (S6) is based on a flat electrode, and therefore it is not suitable for our non-flat structure of the one-dimensional geometry nanorod arrays.[S3] The comparison results of a flat electrode and non-flat structure on obtaining the N_Ds shows that an underestimates the donor density by 20% is achieved for the latter mode when it is considered as the former one.[S3] In our work, the Fe_2O_3-based nanoarrays photoanodes are all non-flat structure, thus the N_D values for them are 20% larger than the experimental results calculated by equation (S7).

6. Calculation of bulk charge separation and surface charge injection efficiency: the measured water splitting photocurrent (J_{H_2O}) can be described as equation (S8):[S4]

$$J_{H_2O} = J_{abs} \times \eta_{separation} \times \eta_{injection} \qquad (S8)$$

in which J_{abs} is the photocurrent density assuming that all absorbed photons can be converted into current (i.e., APCE = 100%), it is a product of the AM 1.5G spectrum and the LHE of the photoelectrode. $\eta_{separation}$ is the separation efficiency of photogenerated holes that reach the electrode/electrolyte interface without recombining with electrons in the bulk. $\eta_{injection}$ is the injection efficiency of photogenerated holes from electrode to electrolyte without being recombined with electrons at surface traps.

In the presence of hole scavenger Na_2SO_3, the surface recombination of charge carriers can be completely suppressed without influencing the charge separation in the electrode bulk (i.e., $\eta_{injection}$ = 100%). Thus, the $\eta_{separation}$ and $\eta_{injection}$ can be calculated as following equations (S9-S10):[21,S4]

$$\eta_{separation} = J_{SO_3^{2-}}/J_{abs} \qquad (S9)$$

$$\eta_{injection} = J_{H_2O}/J_{SO_3^{2-}} \qquad (S10)$$

where J_{H_2O} and $J_{SO_3^{2-}}$ are the photocurrents achieved in the electrolytes of 1 M KOH and 1 M Na_2SO_3 + 1 M KOH, respectively.

In the case of J_{abs}, it can be calculated according to the following equation (S11):[23]

$$J_{abs}(\lambda) = \int N_{ph}(\lambda) \cdot LHE(\lambda) \cdot e \, d\lambda \qquad (S11)$$

where λ is the wavelength (nm), $N_{ph}(\lambda)$ is the photon flux (mW cm^{-2} nm^{-1}), *e* is the elementary charge (e = 1.602×10^{-19}), $LHE(\lambda)$ is the light harvesting efficiency.

7. *Hydrogen and oxygen evolution measurements and faradaic efficiency determination:* the generated hydrogen (H_2) and oxygen (O_2) gases were collected by water drainage method for

Ti:Fe_2O_3 and Ti:Fe_2O_3@GCNNs-CQDs photoanodes under AM 1.5G illumination, and the purity of them was confirmed by gas chromatography (GC) analysis. The area of the working electrodes is 1 cm^{-2}. Then the moles of H_2 and O_2 can be calculated according to the following ideal gas law equation (S12):

$$n = \frac{PV}{RT} \qquad (S12)$$

in which n is the mole of H_2 or O_2 (mol); P is the atmospheric pressure (P = 101325 Pa); R is the universal gas content (R = 8.314 J mol^{-1} K^{-1}); T is the gas temperature (T = 298.15 K).

The faradaic efficiency (η) of Ti:Fe_2O_3 and Ti:Fe_2O_3@GCNNs-CQDs photoanodes for PEC water splitting can be determined by the following equation (S13):[S5]

$$\eta = \frac{zFn}{Q} \qquad (S13)$$

where z is the number of transferred electrons per mole of evolved gas (4 for O_2 and 2 for H_2); F is the Faraday constant (F = 96485 C mol^{-1}); n is the mole of H_2 or O_2 (mol); Q is the passed photogenerated charge (C).

8. Supplemental Figures

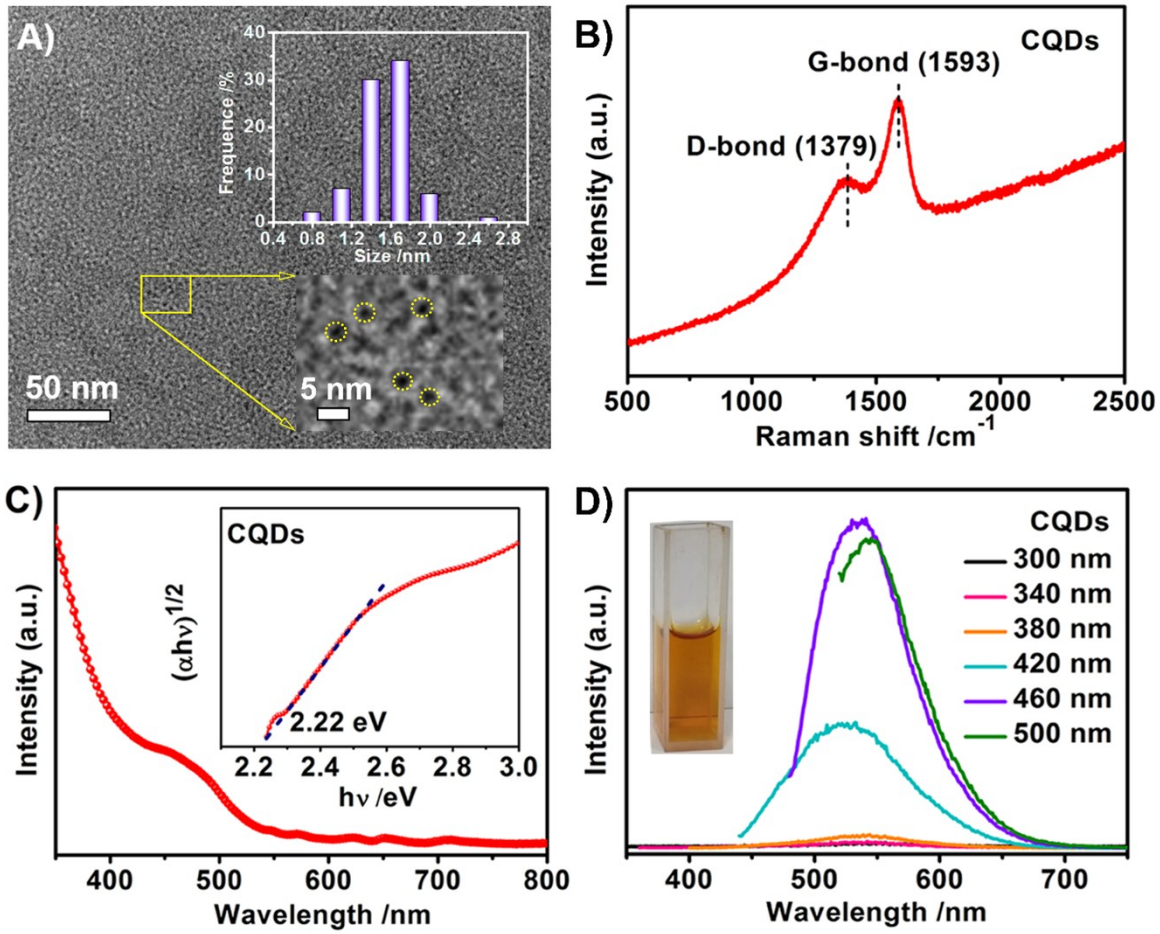

Figure S1. (A) TEM image (inset: the size distribution and the enlarged circled area of CQDs), (B) Raman spectrum, and (C) UV-vis DRS spectrum (inset: the band gap estimation based on the Kubelka-Munk function for CQDs) of CQDs, respectively. (D) PL emission spectra of CQDs with different excitation wavelengths (inset: photograph of CQDs solution), respectively.

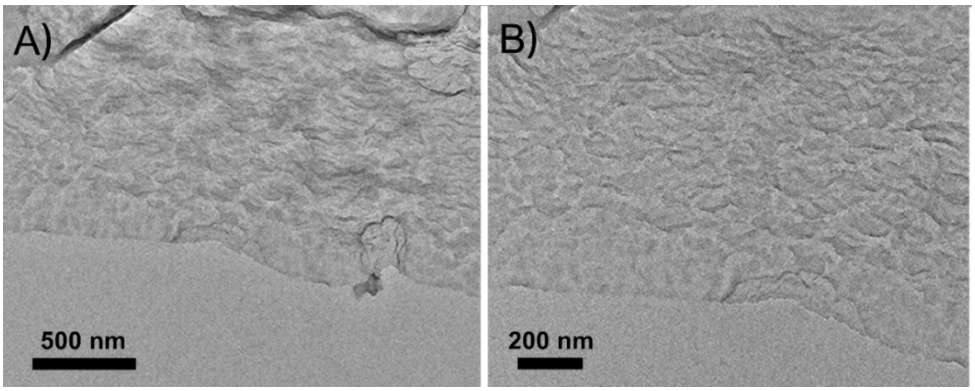

Figure S2. TEM images of (A, B) GCNNs with different magnification.

As shown in Figure S2, graphitic carbon nitride shows the morphology of ultra-thin nanosheets, which can denoted as GCNNs (graphitic carbon nitride nanosheets).

5

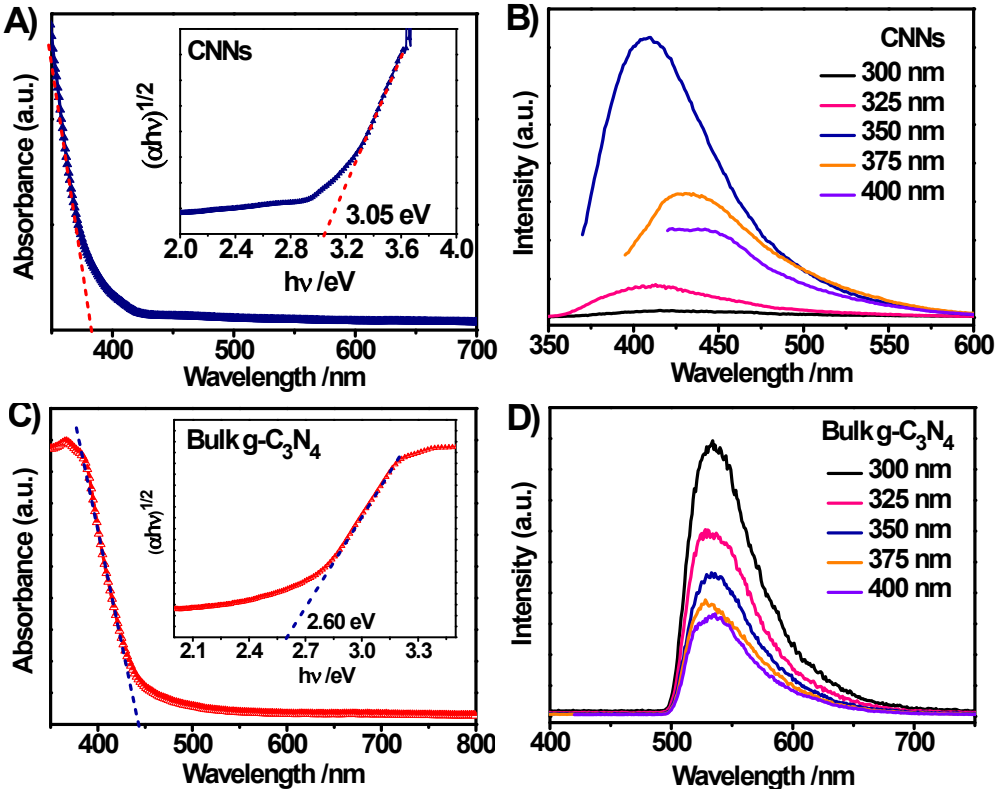

Figure S3. (A) UV-vis DRS spectrum (inset: the E_g estimation based on the Kubelka-Munk function for GCNNs), and (B) PL emission spectra of GCNNs with different excitation wavelengths, respectively. (C) UV-vis DRS spectrum (inset: the E_g estimation based on the Kubelka-Munk function for bulk g-C_3N_4), and (D) PL emission spectra of bulk g-C_3N_4 with different excitation wavelengths, respectively.

As shown in Figures S3A and S3C, GCNNs and bulk g-C_3N_4 show their intrinsic light absorption edges recorded in the wavelength of around 384 and 440 nm, respectively, indicating slightly enhanced band gap of GCNNs with respect to bulk C_3N_4. Notably, the band gap (E_g) values of GCNNs and bulk g-C_3N_4 are estimated to be 3.05 and 2.60 eV, respectively. Furthermore, the PL spectra in Figures S3B and S2D reveal that the emission peaks for GCNNs show blue shift in comparison with the bulk g-C_3N_4.

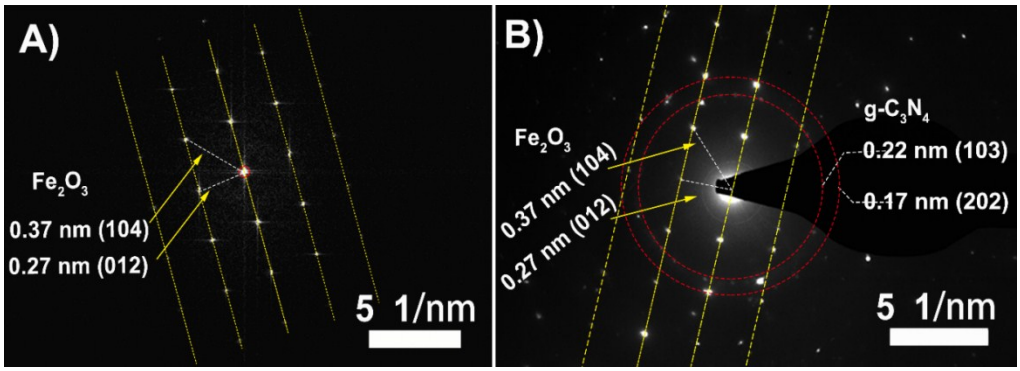

Figure S4. SAED patterns of (A) Ti:Fe_2O_3, and (B) Ti:Fe_2O_3@GCNNs-CQDs, respectively.

The selected area electron diffraction (SAED) images of Ti:Fe_2O_3 and Ti:Fe_2O_3@GCNNs-CQDs are given in Figure S4. Clearly to see, Ti:Fe_2O_3 shows its nature of signal crystalline, two hinds of well-resolved lattice fringes of 0.37 and 0.27 nm corresponding to the (104) and (012) planes of Fe_2O_3 are observed. While in composite of Ti:Fe_2O_3@GCNNs-CQDs specimen, there are not only contain the SAED pattern of Fe_2O_3 but also the g-C_3N_4, strongly suggesting that GCNNs are indeed coated on surface of Fe_2O_3 to form a core-shell structure.

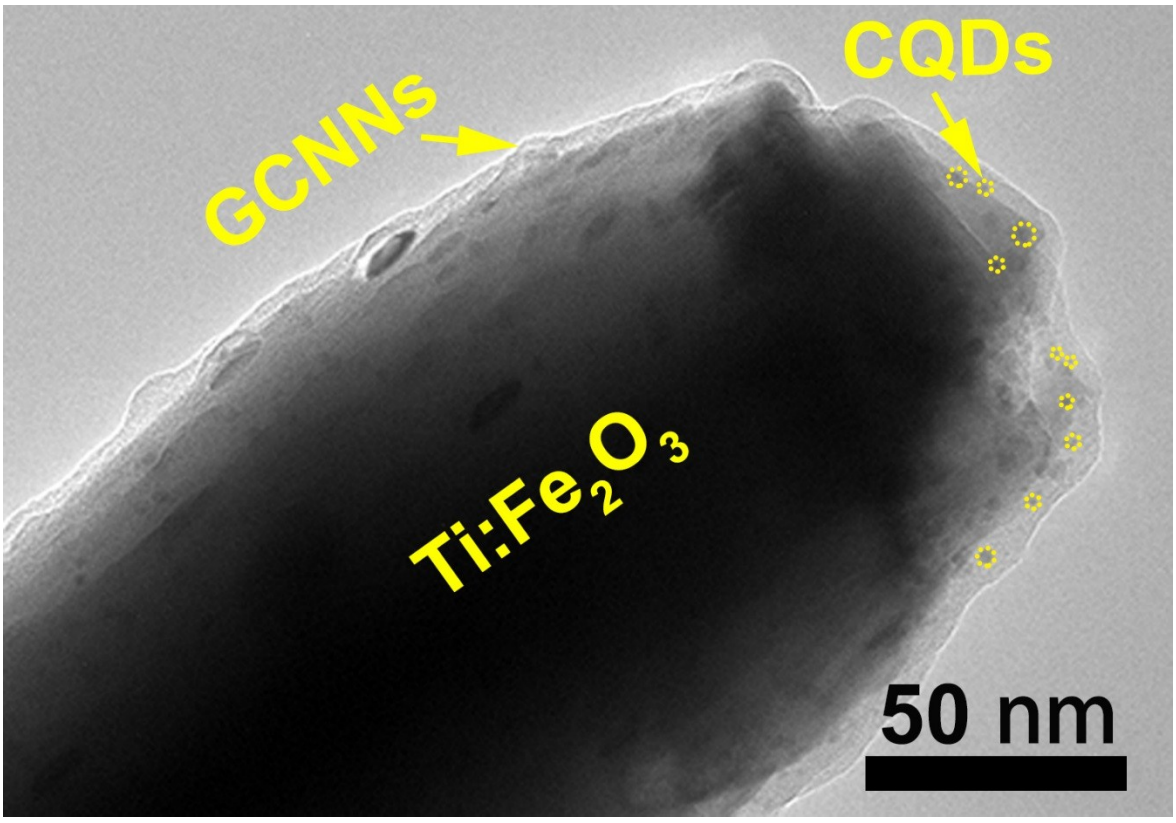

Figure S5. TEM image of Ti:Fe_2O_3@GCNNs-CQDs core-shell structure.

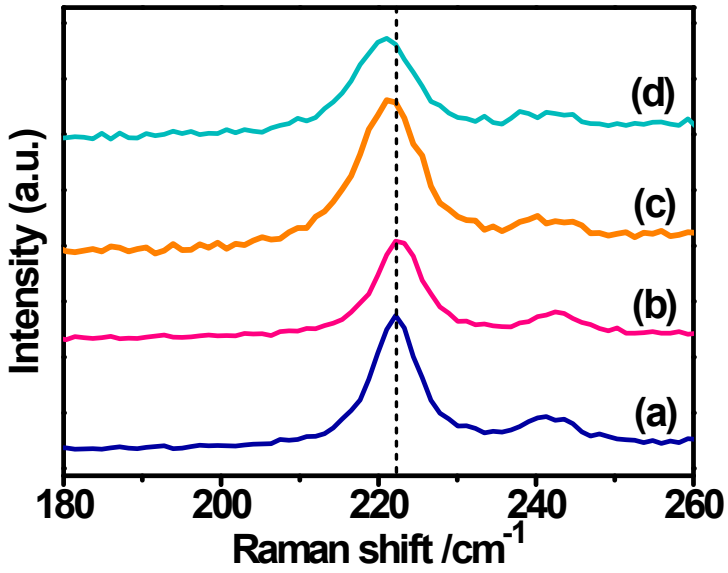

Figure S6. The enlarged view of the Raman spectra in Figure 2B of the main text for Raman shift range from 180 to 260 cm^{-1} over (a) Ti:Fe_2O_3, (b) Ti:Fe_2O_3@GCNNs, (c) Ti:Fe_2O_3/CQDs, and (d) Ti:Fe_2O_3@GCNNs-CQDs specimens.

5

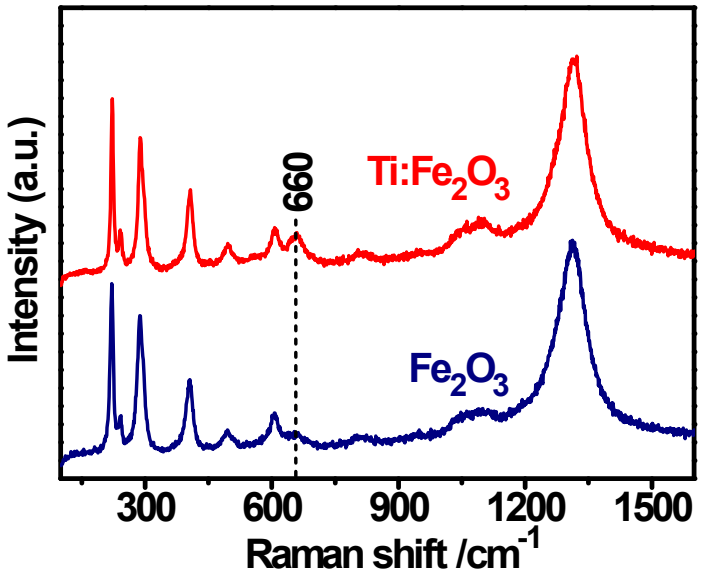

Figure S7. Comparison of the Raman spectra of pristine Fe_2O_3 and Ti:Fe_2O_3.

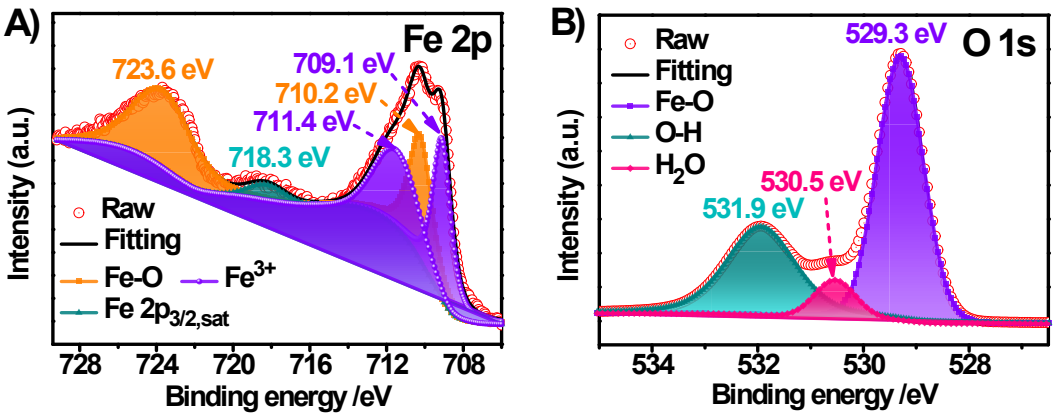

Figure S8. XPS spectra of (A) Fe 2p, and (B) O 1s for Ti:Fe_2O_3 specimen.

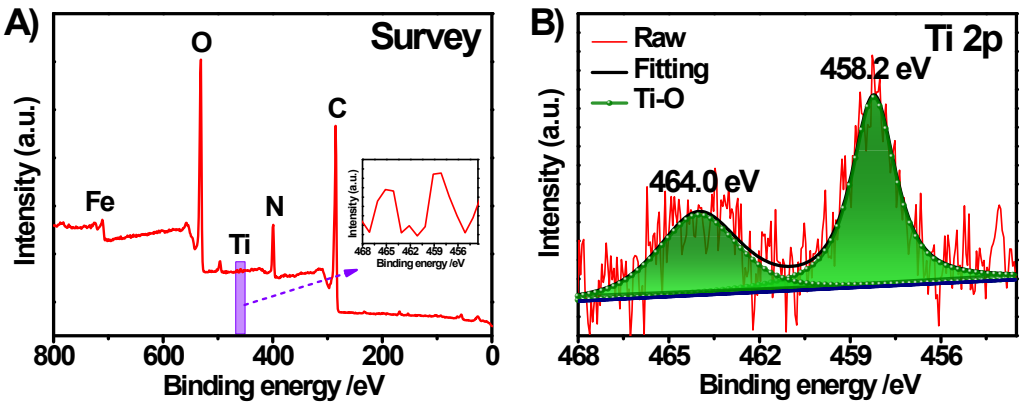

Figure S9. XPS spectra of (A) survey, and (B) Ti 2p for Ti:Fe_2O_3@GCNNs-CQDs photoanode. Inset: the enlarged view of the circled area in (A).

Figure S9A shows the survey scan spectrum of Ti:Fe_2O_3@GCNNs-CQDs, clearly that C, N, Fe, O, and C can be all observed. Figure S9B shows the Ti 2p XPS spectrum, and two remarkable peaks located at 464.0 and 458.2 eV are found, which confirms the existence of Ti^{4+}.[34]

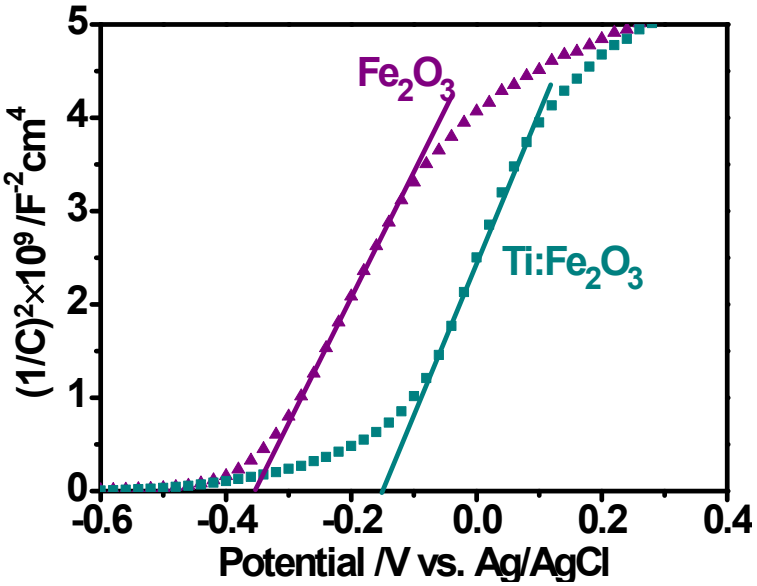

Figure S10. M-S plots of Fe_2O_3 and Ti:Fe_2O_3 photoanodes.

The Mott-Schottky (M-S) plots of pure Fe_2O_3 and Ti:Fe_2O_3 are shown in Figure S10, with their carrier densities (N_Ds) are 1.6×10^{20} and 1.3×10^{20} cm^{-3}, respectively. This result indicate that Ti does not act as an electronic dopant to increase the N_D of Fe_2O_3, but shifts the flat potential (F_{fb}) to much more anodic position in comparison with pure Fe_2O_3, resulting in increased band-bending which process is benefit for charge separation.[14] Here, the Ti maybe enriches in the Fe_2O_3 grain surface. In addition, the Ti-dopant does not change the n-type semiconductor character of Fe_2O_3.

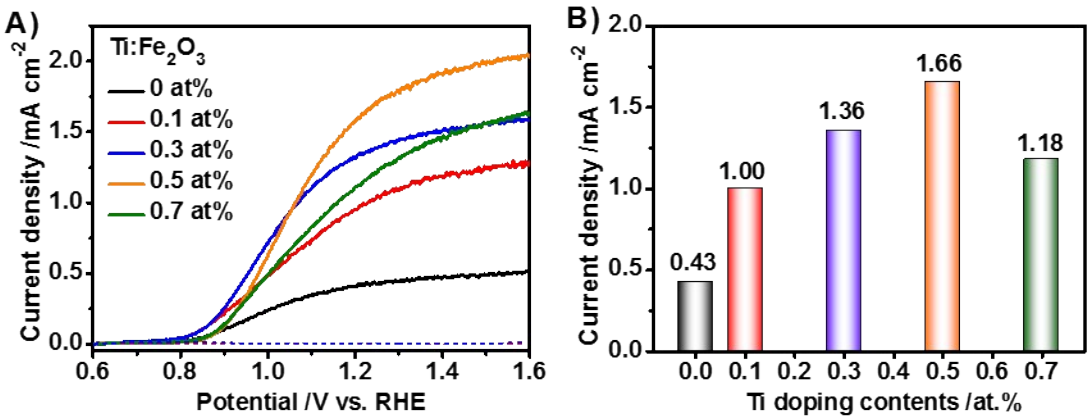

Figure S11. (A) Comparison of the LSV plots of Ti:Fe_2O_3 with various Ti doping concentrations. And (B) the photocurrent density at 1.23 V_{RHE} related to Ti doping concentrations.

5

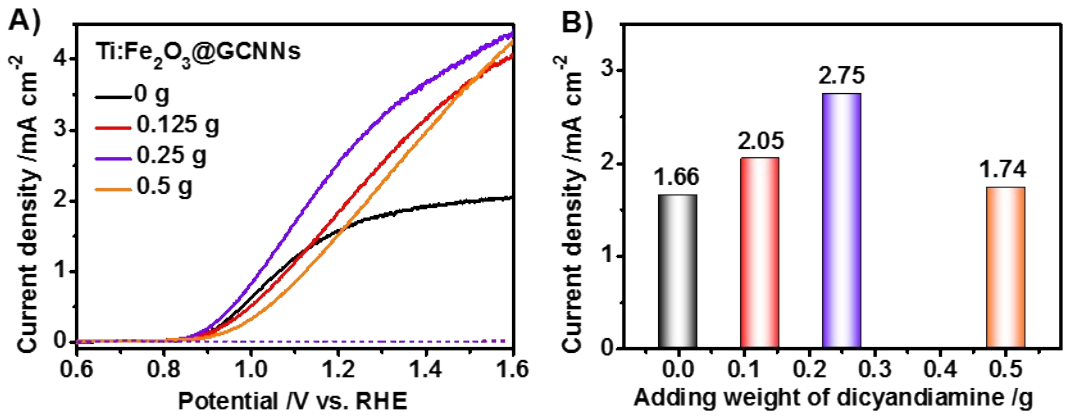

Figure S12. (A) Comparison of the LSV plots of Ti:Fe_2O_3@GCNNs with various GCNNs loading amount. And (B) the photocurrent density at 1.23 V_{RHE} related to adding weight of dicyandiamine.

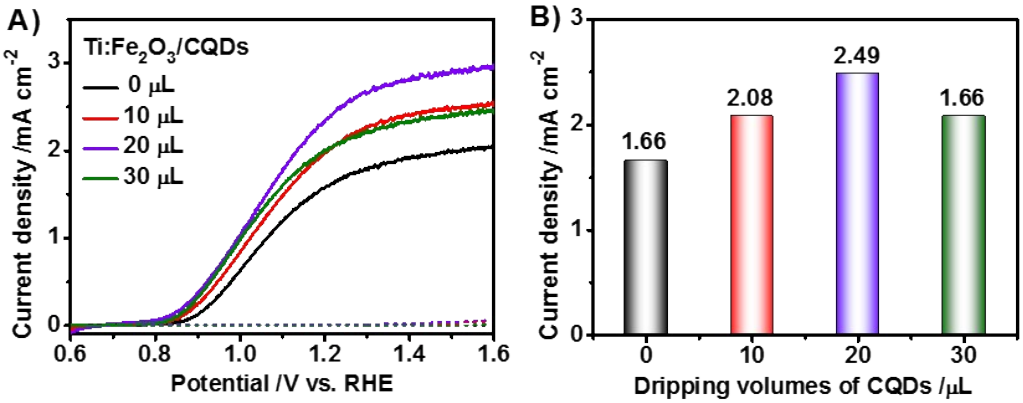

Figure S13. (A) Comparison of the LSV plots of Ti:Fe_2O_3/CQDs with various CQDs loading amount. And (B) the photocurrent density at 1.23 V_{RHE} related to different dripping volumes of CQDs solution.

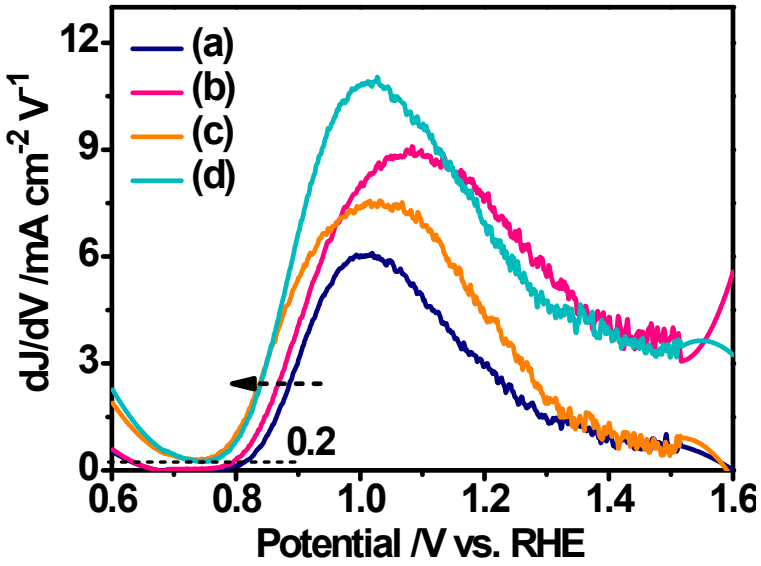

Figure S14. First-order derivative of the photocurrent density as a function of voltage for (a) Ti:Fe_2O_3, (b) Ti:Fe_2O_3@GCNNs, (c) Ti:Fe_2O_3/CQDs, and (d)Ti:Fe_2O_3@GCNNs-CQDs, respectively.

The onset potentials of the photoanodes can be quantitatively valued from the LSV plots by the reported method,[35] with their values at which dJ/dV > 0.2 mA cm^{-2} V^{-1}. As we can see from Figure S14 that the introduction of CQDs can slightly shift the onset potential of the photoanodes to cathodic position.

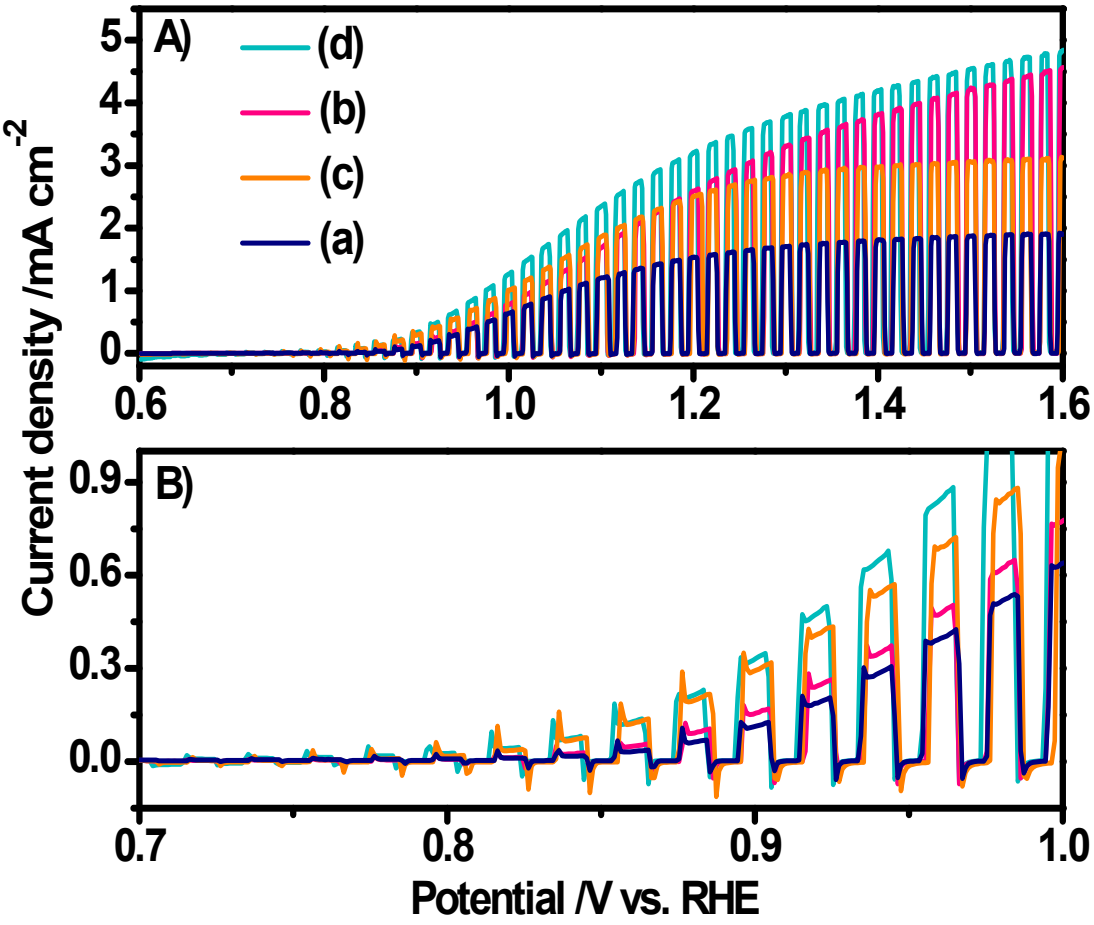

Figure S15. (A) LSV curves under chopped light for (a) Ti:Fe_2O_3, (b) Ti:Fe_2O_3@GCNNs, (c) Ti:Fe_2O_3/CQDs, and (d) Ti:Fe_2O_3@GCNNs-CQDs photoanodes, respectively. The frequency of chopped light is 0.25 Hz. (B) The enlarged view of (A) in the x-axis range of 0.7~1.0 V_{RHE}.

In Figure S15B, the transient spikes for the photoanodes on x-axis range of 0.7~1.0 V_{RHE} are seen more clearly, finding that the Ti:Fe_2O_3/CQDs and Ti:Fe_2O_3@GCNNs-CQDs show slightly the larger transient spikes than that of Ti:Fe_2O_3 and Ti:Fe_2O_3@GCNNs specimens, probably because of the good charge transfer behavior of CQDs as well as its character similar to cocatalyst for collecting holes to arrive to the surface, participating the water splitting reaction.

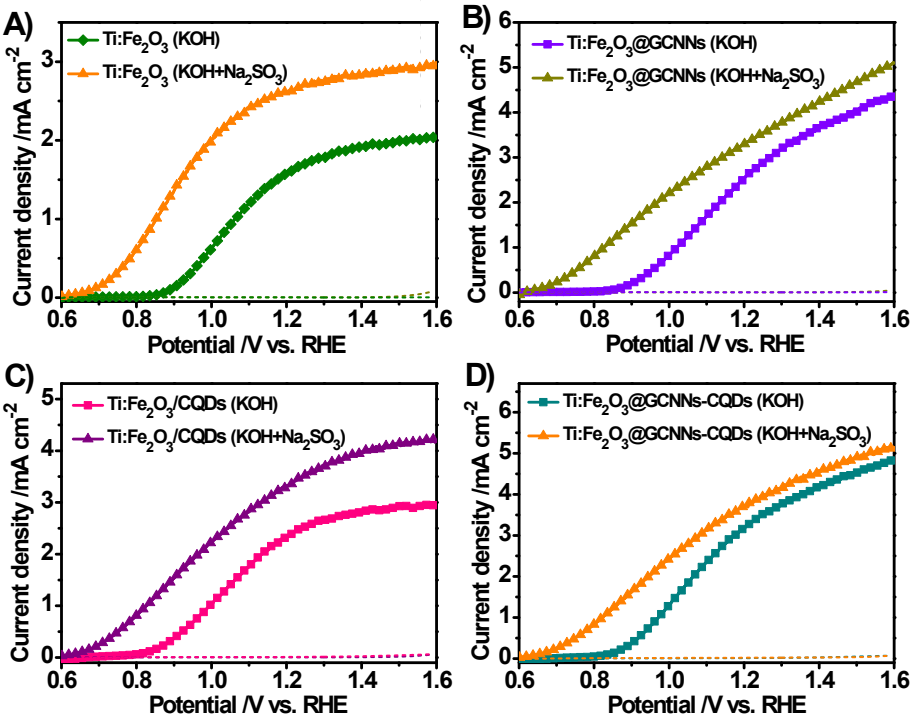

Figure S16. LSV plots of photoanodes in the electrolytes of KOH and KOH + Na_2SO_3 for (A) Ti:Fe_2O_3, (B) Ti:Fe_2O_3@GCNNs, (C) Ti:Fe_2O_3/CQDs, and (D) Ti:Fe_2O_3@GCNNs-CQDs, respectively.

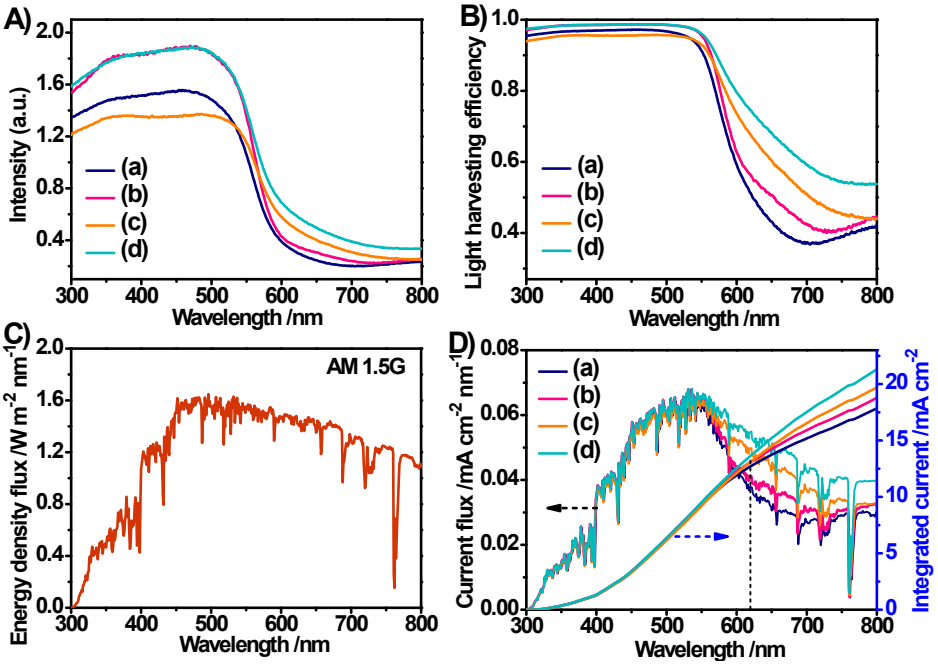

Figure S17. (A) UV-vis DRS and (B) LHE spectra for Ti:Fe_2O_3-based photoanodes of (a) Ti:Fe_2O_3, (b) Ti:Fe_2O_3@GCNNs, (c) Ti:Fe_2O_3/CQDs, and (d) Ti:Fe_2O_3@GCNNs-CQDs, respectively. (C) The energy density flux of the standard solar spectrum of the AM 1.5G. (D) The calculated current density flux and integrated current density (J_{abs}) for (a) Ti:Fe_2O_3, (b) Ti:Fe_2O_3@GCNNs, (c) Ti:Fe_2O_3/CQDs, and (d) Ti:Fe_2O_3@GCNNs-CQDs.

The optical properties of the obtained photoanodes are tested by the ultraviolet-visible diffuse reflectance spectra (UV-vis DRS), as shown in Figure S17A. Clearly, the light absorption edge of Ti:Fe_2O_3 is recorded in the wavelength of around 620 nm, corresponding to a band gap of 2.05 eV. That the absorption ability and light harvesting efficiency (LHE) of Ti:Fe_2O_3 is slightly enhanced after the introduction of CQDs. As results, for Ti:Fe_2O_3 with a band gap of 2.05 eV (Figure S19), the J_{abs} for Ti:Fe_2O_3, Ti:Fe_2O_3@GCNNs, Ti:Fe_2O_3/CQDs, and Ti:Fe_2O_3@GCNNs-CQDs are estimated to be 12.71, 13.08, 13.12, and 13.65 mA cm^{-2}, respectively.

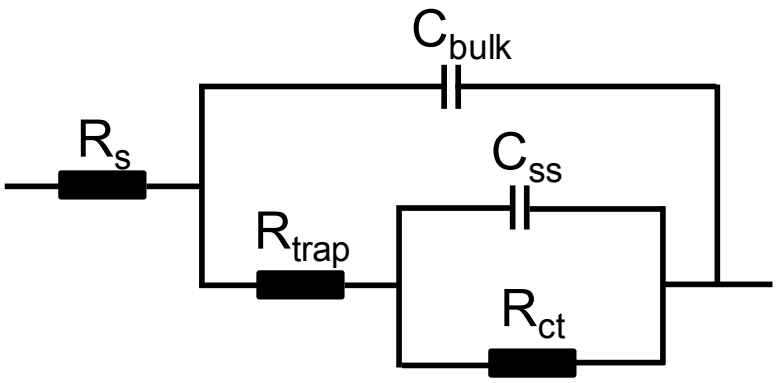

Figure S18. The equivalent circuit model for fitting the EIS spectra.

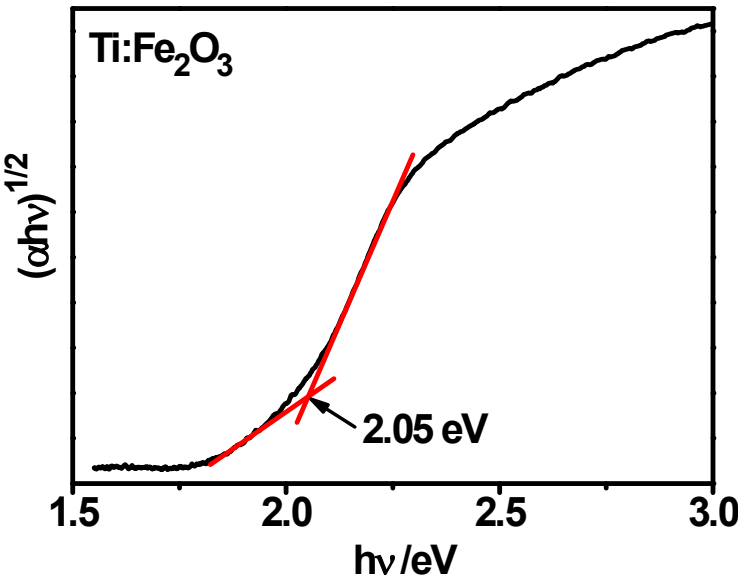

Figure S19. Band gap estimation based on the Kubelka-Munk function for Ti:Fe_2O_3.

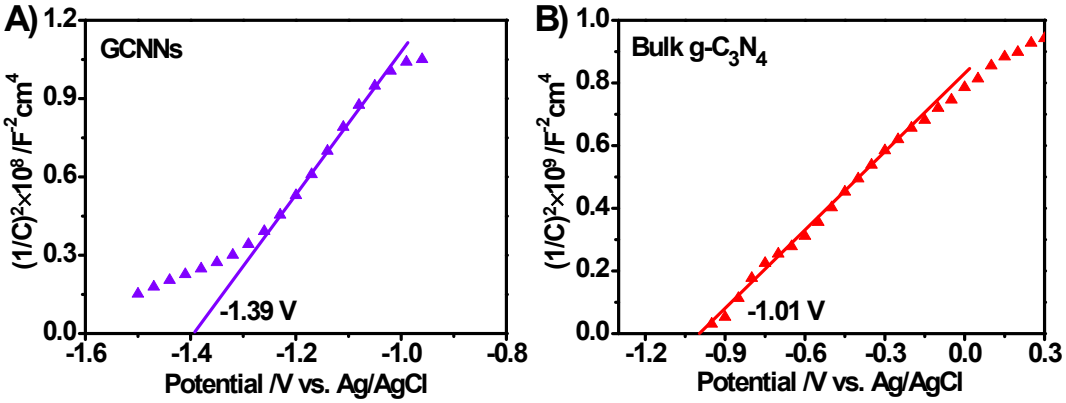

Figure S20. M-S plots of (A) GCNNs and (B) bulk g-C_3N_4 in dark condition.

By comparing the M-S plots of GCNNs and bulk g-C_3N_4 in Figure S20, we can see that GCNNs shows much negative flat potential (E_{fb}) level than that of bulk g-C_3N_4, which are -1.39 and -1.01 V *vs*. Ag/AgCl, respectively. This phenomenon can be ascribed to the quantum confinement effect of GCNNs.[16,22]

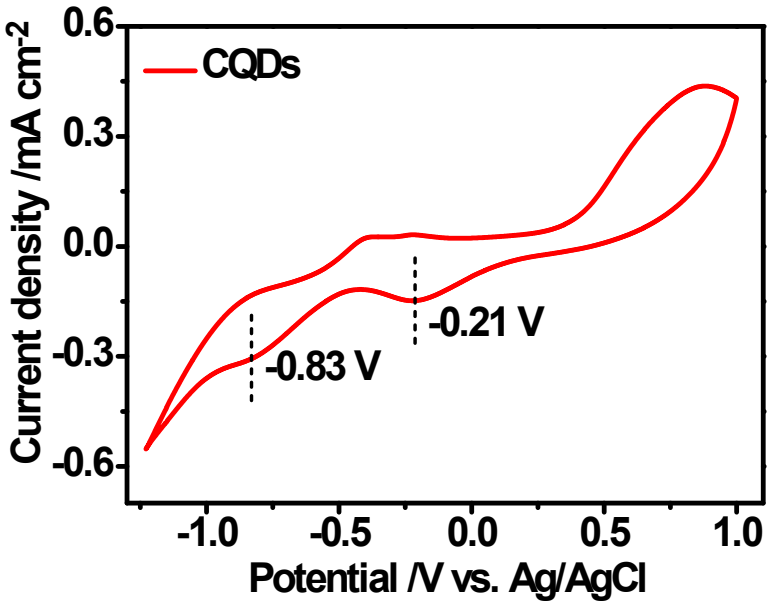

Figure S21. CV curve of CQDs.

As shown in Figure S21, there are two reduction peaks centered at -0.21 and -0.83 V *vs.* Ag/AgCl from the cyclic voltammetry (CV) curve, while the second one can be assigned to LUMO level of CQDs according to the reported value.[S6]

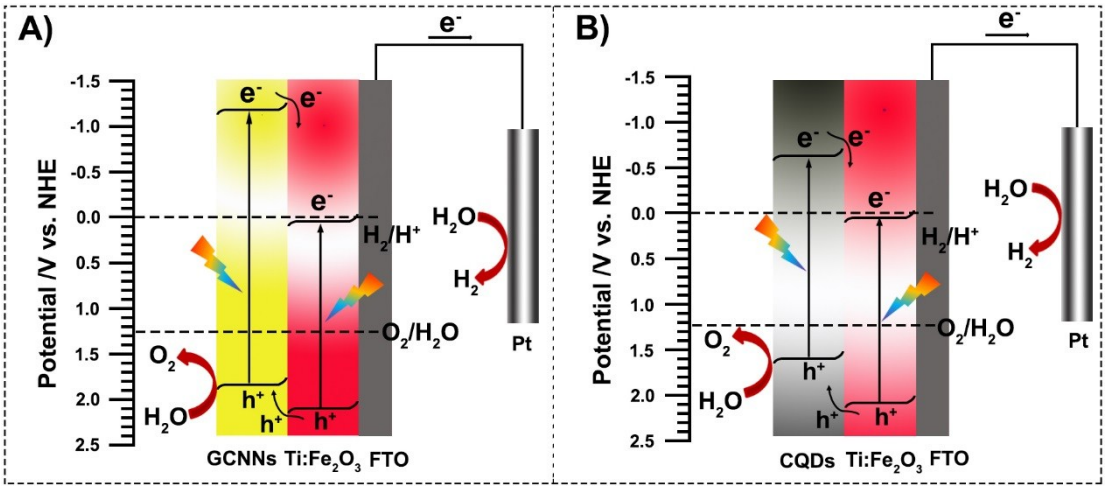

Figure S22. The energy band diagrams of (A) Ti:Fe_2O_3@GCNNs and (B) Ti:Fe_2O_3/CQDs.

As shown in Figure S22A, under AM 1.5G illumination, the energy band diagrams of Ti:Fe_2O_3@GCNNs can be regarded as the type-II heterojunction structure, that the CB-electrons of GCNNs can be transferred to CB of Ti:Fe_2O_3, in the meantime VB-holes of Ti:Fe_2O_3 are flowing to VB of GCNNs. As results, the separation of photogenerated charge carriers on Ti:Fe_2O_3 can be boosted after introduction of GCNNs. For the same taken, the Ti:Fe_2O_3/CQDs also shows their type-II heterojunction structure for water splitting (Figure S22B).

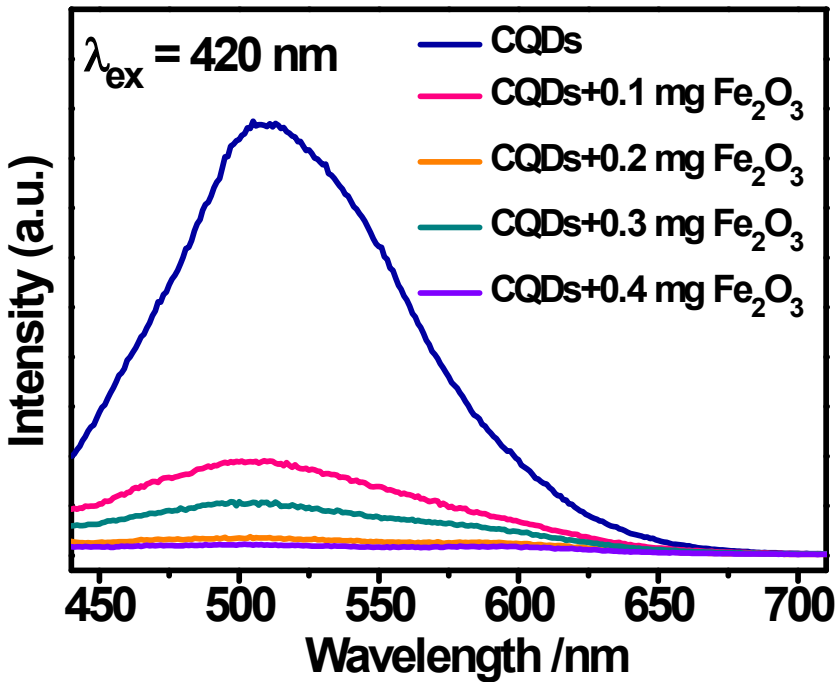

Figure S23. PL spectra of CQDs solution with different weight of Fe_2O_3 under excitation wavelength of 420 nm.

As illustrated in Figure S23, the PL intensity of CQDs solution decreases as the adding amount of Fe_2O_3 increases, showing that CQDs plays positive role in enhancing the separation of photogenerated charge carriers in Fe_2O_3.

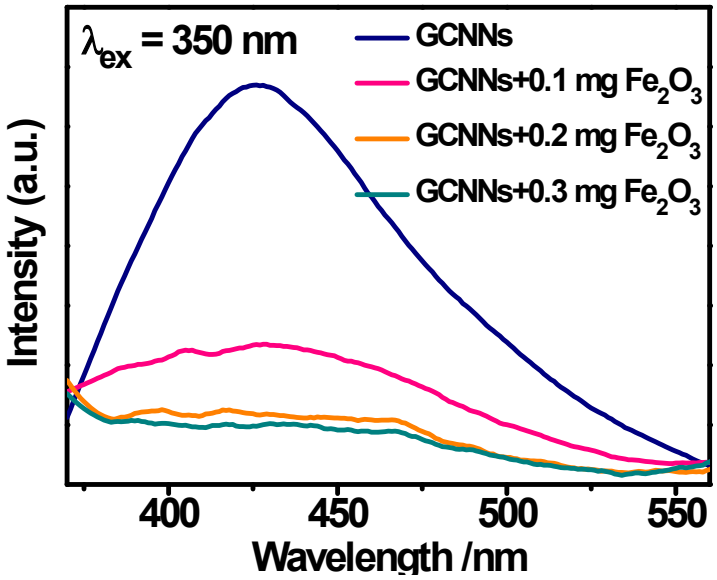

Figure S24. PL spectra of GCNNs solution with different weight of Fe_2O_3 under excitation wavelength of 350 nm.

As illustrated in Figure S24, the PL intensity of GCNNs solution decreases as the adding amount of Fe_2O_3 increases, suggesting the positive role of GCNNs in promoting the separation of photogenerated electron-hole pairs in Fe_2O_3.

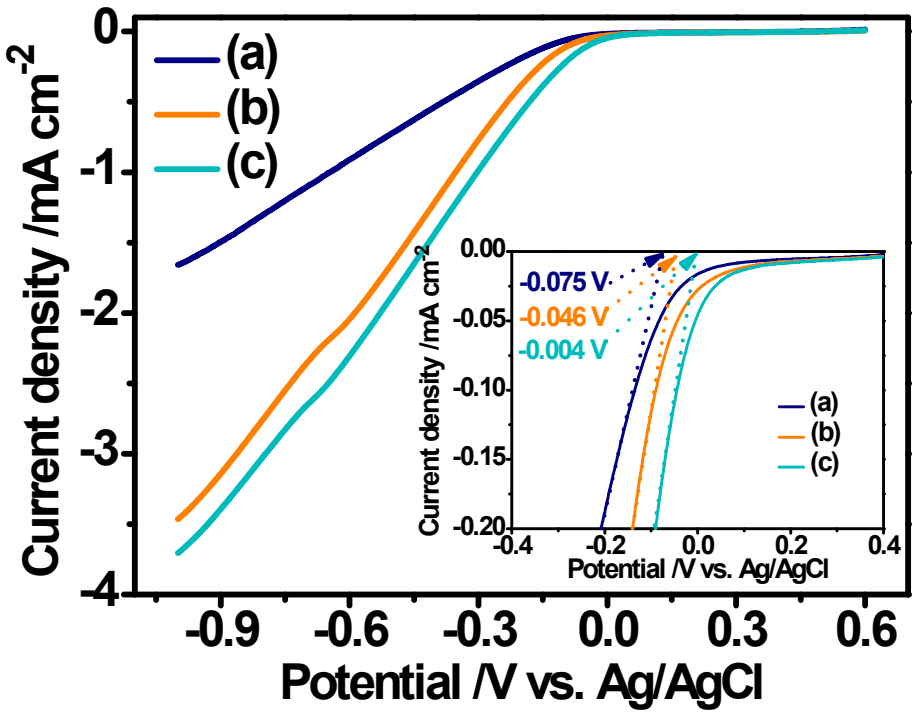

Figure S25. LSV curves of (a) Ti:Fe_2O_3, (b) Ti:Fe_2O_3/CQDs, and (c) Ti:Fe_2O_3@GCNNs-CQDs photoelectrodes in 0.05 M (pH = 7.0) phosphate buffered 25 mM H_2O_2 solution in dark condition.

5

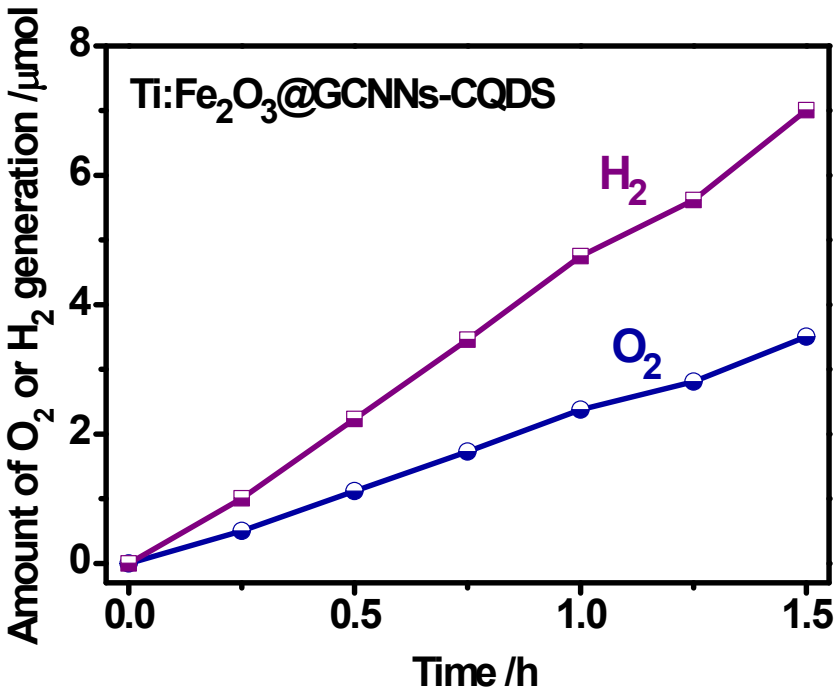

Figure S26. The generation of H_2 and O_2 with Ti:Fe_2O_3@GCNNs-CQDs specimen under AM 1.5G illumination without applying any external potential.

In Scheme 1B in the main text, we propose that the CB-electrons of CQDs are leaved to participate water reduction. To confirm this hypothesis, the photocatalytic H_2 and O_2 generated on Ti:Fe_2O_3@GCNNs-CQDs specimen are collected under AM 1.5G illumination without applying any external potential, as shown in Figure S26. As result, Ti:Fe_2O_3@GCNNs-CQDs can produce H_2 and O_2 concurrently with the O_2 generation rate of 2.3 μmol h^{-1}.

9. Supplemental Tables

Table S1. Comparison of photoelectrochemical performance of Ti:Fe_2O_3@GCNNs-CQDs photoanode obtained in this study with other reprehensive reports on Fe_2O_3-based photoanodes.

Photoanodes	Photocurrent density (mA cm^{-2})	IPCE at 1.23 V_{RHE}	References.
Ti:Fe_2O_3@GCNNs-CQDs	**3.38 at 1.23 V_{RHE}**	**77% at 400 nm**	
Ti:Fe_2O_3/CQDs	**2.49 at 1.23 V_{RHE}**	**59% at 400 nm**	**This work**
Ti:Fe_2O_3@GCNNs	**2.75 at 1.23 V_{RHE}**	**63% at 400 nm**	
C/Co_3O_4/Fe_2O_3	1.48 at 1.23 V_{RHE}	28% at 350 nm	[27]*Angew. Chem. Int. Ed.* 2016, 55, 585
rGO-ITO@Fe_2O_3	3.30 at 1.23 V_{RHE}	33% at 390 nm	[S7]*Nano Energy* 2016, 30, 892
C/Fe_2O_3	2.10 at 1.23 V_{RHE}	52% at 370 nm	[S8]*Energy Environ. Sci.* 2013, 6, 1965
Acid treated Sn-doped Fe_2O_3	1.60 at 1.23 V_{RHE}	28% at 375 nm	[S9]*Angew. Chem. Int. Ed.* 2016, 55, 3403
Co-Pi/Ag/Fe_2O_3	4.68 at 1.23 V_{RHE}	80% at 320 nm	[30]*Adv. Mater.* 2016, 28, 6405
Fe_2O_3/Fe_2TiO_5/$FeNiO_x$	2.70 at 1.23 V_{RHE}	23 % at 300 nm	[S10]*Small* 2016, 12, 3415
Co-Pi/Fe_2TiO_5/Fe_2O_3	2.60 at 1.23 V_{RHE}	40 % at 380 nm	[S11]*ACS Nano* 2015, 9, 5348
Co-Pi/P-doped Fe_2O_3	3.1 at 1.23 V_{RHE}	39 % at 400 nm for P-doped Fe_2O_3	[S12]*Energy Environ. Sci.* 2015, 8, 1231
Au/Si/Fe_2O_3	2.60 (0 V vs. Pt counter electrode)	17% at 850 nm (0 V vs. Pt counter electrode)	[S13]*Nano Lett.* 2014, 14, 18
Co-Pi/Fe_2O_3/NSP arrays	3.05 at 1.23 V_{RHE}	43% at 360 nm	[S14]*Nano Lett.* 2014, 14, 2123
CIO-m/Ti:Fe_2O_3	2.49 at 1.23 V_{RHE}	43 % at 380 nm	[39]*Adv. Funct. Mater.* 2016, *26*, 4414
Co-Pi/Zr-Fe_2O_3	1.87 at 1.23 V_{RHE}	28 % at 300 nm	[S15]*Angew. Chem. Int. Ed.* 2017, 56, 4150
Au/Fe_2O_3/FeOOH	3.2 at 1.23 V_{RHE}	80 % at 390 nm	[S16]*Nano Energy* 2017, 35, 171
FeOOH/TiO_2/Ti:Fe_2O_3	3.1 at 1.23 V_{RHE}	65% at 350 nm	[26]*Angew. Chem. Int. Ed.* 2017, 129, 12967
Ti-(SiO_x/np-Fe_2O_3)/Co-Pi	3.19 at 1.23 V_{RHE}	70% at 440 nm	[S17]*Angew. Chem. Int. Ed.* 2016, 55, 9922
FeOOH/Fe_2O_3	1.21 at 1.23 V_{RHE}	–	[S18]*Angew. Chem. Int. Ed.* 2016, 55, 10854

5

Table S2. The fitting results using the equivalent model for EIS measurements.

Samples	$Ti:Fe_2O_3$	$Ti:Fe_2O_3$@GCNNs	$Ti:Fe_2O_3$/CQDs	$Ti:Fe_2O_3$@GCNNs-CQDs
R_s [Ω]	82	57	48	2.7
R_{trap} [Ω]	589	149	685	30
R_{ct} [Ω]	36960	6229	5099	2876

Table S3. The band gap energy (E_g), energy levels of calculated conduction band (E_{CB}) and valence band (E_{VB}) for Ti:Fe_2O_3, CNQDs and CQDs.

Semiconductors	Band gap energy E_g (eV)	Conduction band E_{CB} (or LUMO) (V *vs*. NHE)	Valence band E_{VB} (or HOMO) (V *vs*. NHE)
Ti:Fe_2O_3	2.05	0.05	2.10
GCNNs	3.05	-1.19	1.86
CQDs	2.22	-0.63	1.59

10. Supplemental references

[S1] X. Yu, P. Yang, S. Chen, M. Zhang and G. Shi, *Adv. Energy Mater*. 2017, **7**, 1601805.

[S2] G. Wang, Y. Ling, D. A. Wheeler, K. E. N. George, K. Horsley, C. Heske, J. Z. Zhang and Y. Li, *Nano Lett.* 2011, **11**, 3503-3509.

[S3] I. Mora-Sero, F. Fabregat-Santiago, B. Denier, J. Bisquert, R. Tena-Zaera, J. Elias and C. Levy-Clement, *Appl. Phys. Lett.* 2006, **89,** 203117.

[S4] H. Dotan, K. Sivula, M. Graetzel, A. Rothschild and S. C. Warren, *Energy Environ. Sci.* 2011, **4**, 958-964.

[S5] H.-i. Kim, D. Monllor-Satoca, W. Kim and W. Choi, *Energy Environ. Sci.* 2015, **8**, 247-257.

[S6] X. Xia, N. Deng, G. Cui, J. Xie, X. Shi, Y. Zhao, Q. Wang, W. Wang and B. Tang, *Chem. Commun.* 2015, **51**, 10899-10902.

[S7] Z. Zhang, C. Gao, Y. Li, W. Han, W. Fu, Y. He and E. Xie, *Nano Energy* 2016, **30**, 892-899.

[S8] J. Deng, X. Lv, J. Gao, A. Pu, M. Li, X. Sun and J. Zhong, *Energy Environ. Sci.* 2013, **6**, 1965-1970.

[S9] Y. Yang, M. Forster, Y. Ling, G. Wang, T. Zhai, Y. Tong, A. J. Cowan and Y. Li, *Angew. Chem. Int. Ed.* 2016, **55**, 3403-3407.

[S10] C. Li, T. Wang, Z. Luo, S. Liu and J. Gong, *Small* 2016, **12**, 3415.

[S11] J. Deng, X. Lv, J. Liu, H. Zhang, K. Nie, C. Hong, J. Wang, X. Sun, J. Zhong and S.-T. Lee, *ACS Nano* 2015, **9**, 5348-5356.

[S12] Y. Zhang, S. Jiang, W. Song, P. Zhou, H. Ji, W. Ma, W. Hao, C. Chen and J. Zhao, *Energy Environ. Sci.* 2015, **8**, 1231-1236.

[S13] X. Zhang, X. Xie, H. Wang, J. Zhang, B. Pan and Y. Xie, *J. Am. Chem. Soc.* 2013, **135**, 18-21.

[S14] Y. Qiu, S.-F. Leung, Q. Zhang, B. Hua, Q. Lin, Z. Wei, K.-H. Tsui, Y. Zhang, S. Yang and Z. Fan, *Nano Lett.* 2014, **14**, 2123-2129.

[S15] C. Li, A. Li, Z. Luo, J. Zhang, X. Chang, Z. Huang, T. Wang and J. Gong, *Angew. Chem. Int. Ed.* 2017, **56**, 4150-4155.

[S16] L. Wang, H. Hu, N. Nhat Truong, Y. Zhang, P. Schmuki and Y. Bi, *Nano Energy* 2017, **35**, 171-178.

[S17] H.-J. Ahn, K.-Y. Yoon, M.-J. Kwak and J.-H. Jang, *Angew. Chem. Int. Ed.* 2016, **55**, 9922-9926.

[S18] J. Y. Kim, D. H. Youn, K. Kang and J. S. Lee, *Angew. Chem. Int. Ed.* 2016, **55**, 10854-10858.